Mon. Not. R. Astron. Soc. **000**, 1–13 (2013) Printed 6 January 2014 (MN LATEX style file v2.2)

Connection between optical and γ-ray variability in blazars

T. Hovatta[1⋆], V. Pavlidou[2,3], O. G. King[1], A. Mahabal[4], B. Sesar[4], R. Dancikova[4], S. G. Djorgovski[4], A. Drake[4], R. Laher[5], D. Levitan[4], W. Max-Moerbeck[6], E. O. Ofek[7], T. J. Pearson[1], T. A. Prince[4], A. C. S. Readhead[1], J. L. Richards[8] and J. Surace[5]

[1] *Cahill Center for Astronomy and Astrophysics, California Institute of Technology, Pasadena CA, 91125, USA*
[2] *Physics Department, University of Crete, PO Box 2208, 71003 Heraklion, Greece*
[3] *IESL, Foundation for Research and Technology-Hellas, PO Box 1527, 71110 Heraklion, Crete, Greece*
[4] *Division of Physics, Mathematics, and Astronomy, California Institute of Technology, Pasadena, CA 91125, USA.*
[5] *Spitzer Science Center, MS 314-6, California Institute of Technology, Pasadena, CA 91125, USA.*
[6] *National Radio Astronomy Observatory, P.O. Box 0, Socorro, NM 87801, USA.*
[7] *Benoziyo Center for Astrophysics, Faculty of Physics, Weizmann Institute of Science, Rehovot 76100, Israel.*
[8] *Department of Physics, Purdue University, 525 Northwestern Ave, West Lafayette, IN 47907, USA.*

arXiv:1401.0538v1 [astro-ph.HE] 2 Jan 2014

Accepted XXX. Received YYY; in original form ZZZ

ABSTRACT

We use optical data from the Palomar Transient Factory (PTF) and the Catalina Real-Time Transient Survey (CRTS) to study the variability of γ-ray detected and non-detected objects in a large population of active galactic nuclei (AGN) selected from the Candidate Gamma-Ray Blazar Survey and Fermi Gamma-Ray Space Telescope catalogs. Our samples include 714 sources with PTF data and 1244 sources with CRTS data. We calculate the intrinsic modulation index to quantify the optical variability amplitude in these samples. We find the γ-ray detected objects to be more variable than the non-detected ones. The flat spectrum radio quasars (FSRQs) are more variable than the BL Lac objects in our sample, but the significance of the difference depends on the sample used. When dividing the objects based on their synchrotron peak frequency, we find the low synchrotron peaked (LSP) objects to be significantly more variable than the high synchrotron peaked (HSP) ones, explaining the difference between the FSRQs and BL Lacs. This could be due to the LSPs being observed near their electron energy peak, while in the HSPs the emission is caused by lower energy electrons, which cool more slowly. We also find a significant correlation between the optical and γ-ray fluxes that is stronger in the HSP BL Lacs than in the FSRQs. The FSRQs in our sample are also more Compton dominated than the HSP BL Lacs. These findings are consistent with models where the γ-ray emission of HSP objects is produced by the synchrotron self-Compton mechanism, while the LSP objects need an additional external Compton component that increases the scatter in the flux-flux correlation.

Key words: galaxies: active – galaxies: jets – galaxies: BL Lacertae objects – galaxies: quasars

1 INTRODUCTION

The extra-galactic γ-ray sky is dominated by active galactic nuclei (AGN). The spectral energy distribution (SED) of AGN can be described by two components, a low energy component from radio to X-rays and a high energy one from X-rays to very high energy γ-rays. The low energy component can be attributed to synchrotron radiation in a relativistic jet while the high energy emission can be either inverse Compton (IC) scattering of low-energy seed photons by the synchrotron emitting electrons or emission through a hadronic process. If the seed photons for the IC scattering are the synchrotron photons, the process is called synchrotron self-Compton (SSC) (e.g. Maraschi et al. 1992; Bloom & Marscher 1996). Alternatively, the seed photons can be external to the jet, for example, from the broad line

⋆ E-mail: thovatta@caltech.edu

© 2013 RAS

region or the molecular torus, in which case the process is called external Compton (EC) (e.g. Dermer & Schlickeiser 1993; Sikora et al. 1994). For a recent study of the SED modelling of AGN, see Böttcher et al. (2013).

If an AGN is viewed with its jet very close to the line of sight, it is called a blazar. Blazars emit brightly over the entire electromagnetic spectrum, and can be further divided based on their optical classification into flat spectrum radio quasars (FSRQs) and BL Lac objects. The optical emission of BL Lac objects is dominated by a strong continuum and they show only weak emission lines. FSRQs have strong emission lines and are thought to have a much denser environment near the black hole. The two classes also differ in their large-scale jet properties. FSRQs are thought to be the beamed counterparts of Fanaroff-Riley type II (FR II) galaxies, which have more powerful jets than the Fanaroff-Riley type I (FR I) galaxies, thought to be the unbeamed counterpart of BL Lac objects (Fanaroff & Riley 1974). However, some recent studies have shown that the division of FSRQs and BL Lacs into FR I and FR II galaxies does not always follow this trend (e.g., Landt & Bignall 2008; Kharb et al. 2010).

Early studies using the Energetic Gamma-Ray Experiment Telescope (EGRET) γ-ray instrument showed that high states in the optical and γ rays are connected (e.g., Wagner et al. 1995a,b; Bloom et al. 1997; Hartman et al. 2001), but detailed comparisons were hindered by the poor sampling of the light curves. The tendency for simultaneous flaring has been confirmed since the launch of the Fermi Gamma-Ray Space Telescope (hereafter, *Fermi*) in 2008 and the capability of its Large Area Telescope (LAT) (Atwood et al. 2009) to detect AGN even in their non-flaring states. Many individual sources studied in great detail have shown correlated flares in optical and γ-ray spectral regions (e.g., Bonning et al. 2009; Marscher et al. 2010; Abdo et al. 2010a; Agudo et al. 2011; Ackermann et al. 2012b).

While individual sources have been studied in detail, the number of studies including multiple sources is limited. Chatterjee et al. (2012) studied the 6 best sampled blazars observed within the SMARTS blazar monitoring program and found short delays between the optical and γ-ray flares. By decomposing the optical and γ-ray light curves in to individual flares they also found the shapes of the flares to be similar in the two bands. However, Bonning et al. (2012) studied 12 sources in the same program and found that in some sources the variations were correlated while in others they were not.

A statistical approach was taken by Arshakian et al. (2012) who studied 80 LAT-detected objects in the MOJAVE sample. Using non-simultaneous optical data, they found the optical and γ-ray luminosities to be correlated in the FSRQs in their sample, while no significant correlation was found for BL Lac objects. The dispersion in the optical to γ-ray luminosity correlation was also much larger than for radio and γ-ray luminosities. They attributed this to the possible larger variability in the optical compared to radio, which would increase the scatter in non-simultaneous correlations.

We use the data for 714 AGN in the Palomar Transient Factory (PTF) (Rau et al. 2009) and 1244 AGN in the Catalina Real-Time Transient Survey (CRTS) (Drake et al. 2009) to study the connection between the optical and γ-ray emission in a *population* of AGN. The data sets have 637 sources in common. We use the intrinsic modulation index (Richards et al. 2011) to study differences between sub-populations of sources and the significance estimation method of Pavlidou et al. (2012) to evaluate the flux – flux correlation between the optical and γ-ray data.

Our paper is organized as follows. In Sect. 2 we describe our sample selection and data reduction. Sections 3 and 4 show the results of our analysis. We discuss our results in the context of AGN models in Sect. 5 and summarize our conclusions in Sect. 6

2 SAMPLE AND DATA REDUCTION

We use the AGN sample defined by (Richards et al. 2011) and monitored by them at 15 GHz at the Owens Valley Radio Observatory (OVRO) 40-m as the starting point for our analysis. This sample of 1771 objects includes 1158 sources from the Candidate Gamma-ray Blazar Survey (CGRaBS) (Healey et al. 2008) and all the sources above declination -20° that have been detected by the LAT in the first and second AGN catalogs (Abdo et al. 2010b; Ackermann et al. 2011). The OVRO sample also includes a small number of objects with interesting jet properties or that are being monitored by other programs.

The CGRaBS sample is a statistically well-defined sample that was selected to resemble blazars that were detected by EGRET. The sources were selected from a flat-spectrum parent sample that is complete to 65 mJy flux density at 4.8 GHz and have radio spectral index[1] $\alpha > -0.5$. The CGRaBS sources were then selected based on their radio spectral index, 8.4 GHz flux density, and X-ray flux from *ROSAT* All Sky Survey. The sample was compiled before the launch of *Fermi* and was expected to contain a large number of sources that would be detected by *Fermi*. However, *Fermi* is much more sensitive to hard γ-ray spectrum sources than EGRET and a large number of CGRaBS sources have not been detected by *Fermi*. This makes the sample ideal for studying the differences between the *Fermi*-detected and non-detected objects. Our PTF and CRTS samples contain 508 and 839 CGRaBS sources, respectively. We emphasize that while our samples do not include all CGRaBS sources, they are *unbiased* subsets of the complete sample as the sample selection was not done based on the optical or γ-ray properties of the sources.

We search for all the objects within $1.5''$ of our sample targets in the PTF and $3''$ in the CRTS. These limits were selected based on the pixel size and typical seeing of the observations. We describe the details of the data extraction and analysis for each survey individually below. To allow for comparison with simultaneous OVRO and *Fermi* observations, we use data from 2008 to 2013. The redshifts for the sources in our sample range from 0.04 to 3.9 with a median of 1. For the population studies we divide our final samples into γ-ray loud and quiet objects based on their LAT detection. We use only the sources in the CLEAN samples of the 1st and 2nd LAT AGN catalogs (Abdo et al. 2010a;

[1] here and throughout the paper we define the spectral index as $S \propto \nu^{\alpha}$

Ackermann et al. 2011). These are sources for which only a single association has been determined in the *Fermi* catalogs.

Additionally, we study the differences between the FSRQ and BL Lac objects. The classifications we use come mainly from the CGRaBS and *Fermi* catalogs. Furthermore, we divide the sources based on the frequency of their synchrotron peak ν_p into low synchrotron peaked (LSP), intermediate synchrotron peaked (ISP) and high synchrotron peak (HSP) objects. We use the classifications from the 2nd LAT AGN catalog where the LSP sources have $\nu_p < 10^{14}$ Hz, ISPs have $10^{14} < \nu_p < 10^{15}$ and HSPs have $\nu_p > 10^{15}$ Hz (Ackermann et al. 2011). The number of sources in each subsample is listed in Table 1.

2.1 PTF data

The Palomar Transient Factory is designed to observe optical transients and variable sources. It uses the 48-inch Samuel Oschin Telescope at Palomar Observatory with R- and g′-band filters and a wide-field camera having a 7.2 square degree field of view. For a detailed description of the project and its primary science goals see Law et al. (2009) and Rau et al. (2009). We find PTF R-band data for 870 objects in our sample. The limiting magnitude is about 20.5. Due to the nature of the PTF observations, some areas of the sky get better coverage than others and therefore the number of data points for each source depends on the sky position and varies from less than 10 to a few hundred.

We use the PTF Photometric Pipeline to extract the magnitudes. Images are processed using "standard" reduction procedures, including de-biasing, flat-fielding, and astrometric calibration. Catalogs are generated using SExtractor (Bertin & Arnouts 1996). The PTF data are photometrically calibrated against the SDSS catalog. Photometric nights are used in order to calibrate the photometry all over the PTF footprints to accuracy of 2% (Ofek et al. 2012a,b). In addition, we apply relative calibration to the photometry, with typical precision of a few millimagnitudes at the bright end (magnitude 15). The relative photometry algorithm is described in Ofek et al. (2011).

We discard data based on various flags given by the SExtractor (e.g., blending of multiple sources within the field, bad astrometry of the field) and additional flags given by the PTF Photometric Pipeline (e.g., saturated or dead pixels). The sources can be observed up to four times each night and we average the magnitudes over each night. This is important because our variability analysis method assumes subsequent observations to be independent and multiple observations within a night may introduce biases. We acknowledge that AGN can be variable on time scales less than a day (e.g., Wagner & Witzel 1995) but the variability amplitude is typically a fraction of a magnitude. For our further analysis we select all the objects that have at least three data points. By visually examining all the light curves, we also discarded sources which clearly suffered from blending even if the data were not flagged by SExtractor. This results in a sample of 714 sources which are listed in Table 5.

We correct the PTF R-band magnitudes for Galactic extinction using the re-calibrated dust maps of Schlafly & Finkbeiner (2011) with the reddening law of Fitzpatrick (1999) extracted from NASA/IPAC Extragalactic Database (NED). The corrected magnitudes were then converted into flux density units (mJy) by using a zero point of 3631 Jy. We note that there is an additional colour term correction that affects the conversion (Ofek et al. 2012a) but it is less than 0.04 mag for a typical blazar spectrum and therefore ignored. In all our further analysis we use the light curves in flux density units.

2.2 CRTS data

The Catalina Real-Time Transient Survey[2] uses the data from the Catalina Sky Survey (CSS)[3] to report on optical transients. Observations are made without a specific filter with the 0.68-m Catalina Schmidt Telescope in Arizona, USA, the 0.5-m Uppsala Schmidt at Siding Spring Observatory, NSW, Australia, and the 1.5-m reflector located on Mt. Lemmon in Arizona. The main science goal of CSS is to detect near-Earth objects but the large sky coverage makes it ideal for transient studies. For details of the CRTS and the first results see Drake et al. (2009), Mahabal et al. (2011), and Djorgovski et al. (2012). We find CRTS data from the Catalina Surveys Data Release 2 (Drake et al. 2009) for 1335 sources in our sample. The magnitudes for all the sources are derived using the SExtractor program. The limiting magnitude of CRTS is about 21.

We discard data using the blend flag of SExtractor which indicates if the source is blended with another one in the field. Because the pipeline is not optimized for AGN studies, there are many outliers in the data even after the basic flagging. Outliers have a significant effect on our modulation index analysis, so we discard the most extreme cases. All the sources are observed four times each night within ~ 30 min time period. We use this additional information to discard any data points which differ by more than 0.8 magnitudes from the other data points over the same night, and all the data over a night if the standard deviation of the data points exceeds 0.5 mag. These limits were empirically determined from the data to exclude high outliers that are unlikely to be due to intra-night variability. In the same way as for the PTF data, we average all the observations within a single night. We then select all the sources with at least three data points which results in a sample of 1244 objects. All the sources are listed in Table 6.

For the modulation index study we must convert the magnitudes into flux density units. In the case of the CRTS data this is not straightforward because the observations are done without a filter. However, the setup used resembles a V-band magnitude and it has been empirically determined that the CRTS magnitudes can be converted into Cousins V-band by the relation[4] $V = V_{\rm CSS} + 0.91 \times (V-R)^2 + 0.04$ where $(V-R)$ depends on the spectrum of the object. Because the $(V-R)$ colour varies depending on the flux state of the object (e.g., Bonning et al. 2012), and is unknown for a large fraction of the sources in our sample, we take a statistical approach in the conversion. Jester et al. (2005) derive an empirical relation $(V-R) = 0.38 \times (r-i) + 0.27$ applicable for quasars at redshifts < 2 using the SDSS data.

[2] http://crts.caltech.edu
[3] http://www.lpl.arizona.edu/css/
[4] http://nesssi.cacr.caltech.edu/DataRelease/FAQ2.html

Table 1. Number of sources in the PTF and CRTS samples for the various subsamples used in the analysis. There are 637 sources in common between the two samples.

Sample	All	γ-ray loud	γ-ray quiet	FSRQ	BL Lac	LSP	ISP	HSP
PTF	714	313	401	448	168	127	39	68
CRTS	1244	543	701	717	293	193	67	131

We extract $(r-i)$ colours for 10 000 quasars using the SDSS DR5 sky server SQL tool[5] to obtain a mean value of 0.34 for the $(V-R)$ of quasars. We use this value to convert the CSS magnitudes into Cousins V-band magnitudes, and a zero point of 3953 Jy to convert into mJy. There are 123 sources in our CRTS sample with redshift larger than 2, which are outside the nominal redshift range for the conversion. We note that finding the exact conversion factor is not critical because the multiplicative factor will cancel out in the calculation of the modulation index. However, this will have an effect on the flux-flux correlation and therefore we only use the PTF data in the correlation analysis.

3 INTRINSIC MODULATION INDEX

Variability amplitudes in light curves can be studied in numerous ways, for example using the variability index (e.g., Aller et al. 1992), the fractional variability amplitude (e.g., Edelson et al. 2002), and the modulation index (e.g., Kraus et al. 2003). While all these methods are widely used, they do not account for the effects of irregular sampling and are often applicable only when the variations significantly exceed the measurement errors. Furthermore, they do not provide an estimate of the error in the variability measure.

The intrinsic modulation index $\overline{m}$ was first defined and used in Richards et al. (2011) on the OVRO 40-m 15 GHz data. Its basic principle is the same as the standard modulation index, defined as the standard deviation of the flux density measurements in units of the mean flux density. The main difference is that it is calculated using the intrinsic standard deviation σ_0 and the intrinsic mean flux density S_0 of the observation so that

$$\overline{m} = \frac{\sigma_0}{S_0}. \quad (1)$$

The term intrinsic denotes values that we would obtain if we had zero observational errors and infinite number of samples. The intrinsic values are calculated using a likelihood approach which assumes the observed flux densities to follow a normal distribution with Gaussian errors. The measurement errors are accounted for in the calculation of the joint likelihood for S_0 and $\overline{m}$. For full derivation of the likelihoods see Richards et al. (2011).

The main advantage of this method is that it is possible to determine an uncertainty for the modulation index which is needed in the comparison of the different source populations. For sources with $\overline{m}$ within 3σ of zero, the 3σ upper limit will be determined. Another advantage is that the number of data points in each light curve is accounted for in the errors of $\overline{m}$ so that for sources with fewer data points the errors will be larger. The minimum number of data points needed for the analysis is three. The intrinsic modulation indices and the intrinsic flux densities are listed for each source in the PTF sample in Table 5 and in Table 6 for the CRTS sample.

There are some important limitations with the method and the data that are illustrated in Fig. 1, which shows the intrinsic modulation index plotted against the intrinsic mean flux density of each object. One limitation is the systematic errors in the data sets. It is often the case that sources that are supposed to be constant in flux density will show non-zero modulation index due to systematic uncertainties in the data. In order to test this effect on the PTF and CRTS data, we use data for white dwarfs, which are assumed to be constant in the optical band, to determine the limit above which the variations we detect are due to intrinsic changes in the object and not due to systematic uncertainties. In the PTF data, the highest intrinsic modulation index for a white dwarf at a flux density above 0.3 mJy (see below for the justification of this cutoff) is $\overline{m} = 0.035 \pm 0.002$ and therefore we set the lower limit of the intrinsic modulation index to 0.04 for PTF blazars. Similarly, in the CRTS data the highest value for a white dwarf at high fluxes is $\overline{m} = 0.078 \pm 0.02$ and we set the lower limit to 0.08 for the CRTS blazars.

For sources weaker than a certain flux density limit, the method gives mainly upper limits and shows that below the weak flux density limit, we cannot reliably determine the intrinsic modulation index. This limit is 0.1 mJy for the PTF and CRTS samples, estimated such that we include as few marginal non-detections as possible (i.e. sources with very high upper limits on the intrinsic modulation index). This limit is also required because the white dwarfs show a dependency on the flux density so that at lower fluxes the limit for modulation index is higher, indicating that the errors in the data are underestimated at low fluxes, making the intrinsic modulation index estimates unreliable. These limits are shown in Fig. 1 as yellow hatched regions.

There is also a large concentration of upper limits in both plots at the lower left corner (cyan hatched region in Fig. 1). This is a region where we cannot reliably determine the intrinsic modulation index for sources that are fainter than 0.3 mJy in the PTF sample and 0.5 mJy in the CRTS sample. This effect disappears when the modulation index is above 0.15 for the PTF sample and 0.25 for the CRTS sample. In the following population studies we will exclude the regions outside these limits (yellow and cyan hatched regions in Fig. 1) to ensure that our results are not biased due to incomplete sampling in these regions. We note that our analysis is not sensitive to the exact value of the limits, and we have tested that even 50% higher flux density and modulation index limits would not change any of our conclusions. After these cutoffs and excluding the upper limits

[5] http://cas.sdss.org/dr5/en/proj/advanced/quasars/query.asp

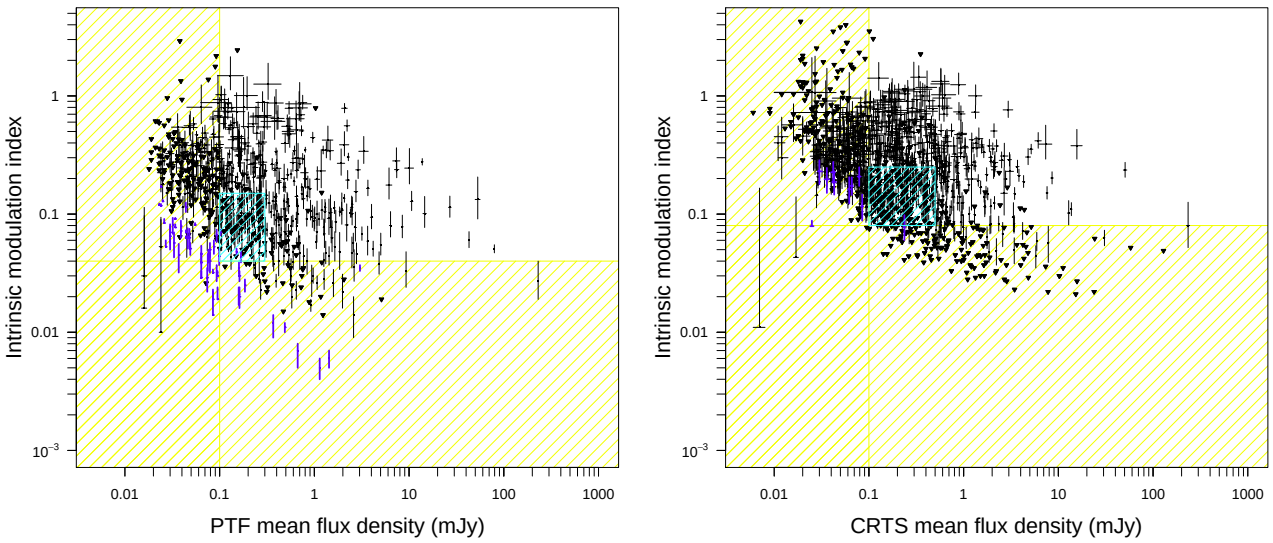

Figure 1. Intrinsic modulation index $\overline{m}$ with 1 σ uncertainty plotted against the intrinsic mean flux density S_0 of all the sources in the PTF (left) and CRTS (right) samples. Black triangles are 3 σ upper limits of $\overline{m}$. Thick blue symbols are white dwarfs used as calibrators. Yellow and cyan hatched areas show the regions not included in the population studies. See the text for details.

we have 271 sources in the PTF sample and 343 sources in the CRTS sample.

Additional caveats for the method are listed in Richards et al. (2011). One of the most important is the assumption of Gaussian flux density distributions and the leakage of probability density to negative flux densities when this is not met. It is clear that the flux density distribution for many of our sources is non-Gaussian, especially when there are only a few data points. This results in long tails in the probability density distribution that in the case of high $\overline{m} \geq 0.5$ leak to unphysical negative flux densities. We estimate that for sources with $\overline{m} \geq 0.7$ about 8% of the "true flux density" probability density leaks to negative values. For sources with $\overline{m} \geq 1.0$ this becomes $\sim 17\%$. There are 21 sources in the PTF sample and 73 in the CRTS sample with $\overline{m} >= 0.7$. The solution to this problem is to extend the likelihood analysis to other shapes of flux density distributions and will be presented in a forthcoming publication.

3.1 Redshift dependence

The redshift range for γ-ray-detected sources is limited due to the capability of *Fermi* to detect sources at high redshifts. Similarly, BL Lac objects have typically lower redshifts than FSRQs. In Fig. 2, we show $\overline{m}$ against the redshift for the *Fermi*-detected and non-detected FSRQs and BL Lacs in both PTF and CRTS samples. The redshift range for *Fermi*-detected sources extends to about $z = 2$ and the redshift range of BL Lacs to $z \sim 1$ while the non-detected sources and FSRQs have a range of redshifts up to almost 4.

We have searched for correlations between $\overline{m}$ and redshift using the non-parametric Kendall's tau test. FSRQs do not show any significant correlations in the data. In BL Lacs there is no significant correlation if we limit the redshifts to $z < 1$. Above this limit the redshifts of BL Lacs are incomplete (e.g. Shaw et al. 2013) and the correlation is biased. As shown in Sect. 3.4 below, the mean intrinsic modulation indices for FSRQs at $z < 1$ and $z > 1$ are similar to within 1σ, showing that there is no redshift dependence. These results show that our conclusions are not affected by the different redshift range of the populations, but for completeness, in the following analysis of γ-ray detected and non-detected sources, and BL Lacs and FSRQs, we show the results for both the total sample and samples restricted to a common redshift range.

3.2 Mean intrinsic modulation index

In the following sections we will investigate whether the intrinsic modulation index correlates with various physical properties of the objects, such as the γ-ray detection, optical classification, and location of the synchrotron peak. We do this using a maximum likelihood approach which is described in Richards et al. (2011). As shown in Fig. 3 the distribution of $\overline{m}$ for the sources approximately follows an exponential function. This allows us to calculate the probability density of the mean intrinsic modulation index m_0. The errors of m_0 are determined from the probability density distribution and they do not have to be symmetric. We can then compare the means of the various sub-populations and determine whether they agree within some significance limit. We consider a result significant at the 3σ level if the p-value is less than 0.0027. The mean intrinsic modulation indices for each sub-population are listed in Table 2.

In order to study the difference between the populations, we calculated the likelihood of the difference between the mean intrinsic modulation indices in the two populations by taking the cross-correlation of the individual m_0 likelihoods for each population. This allows us to estimate

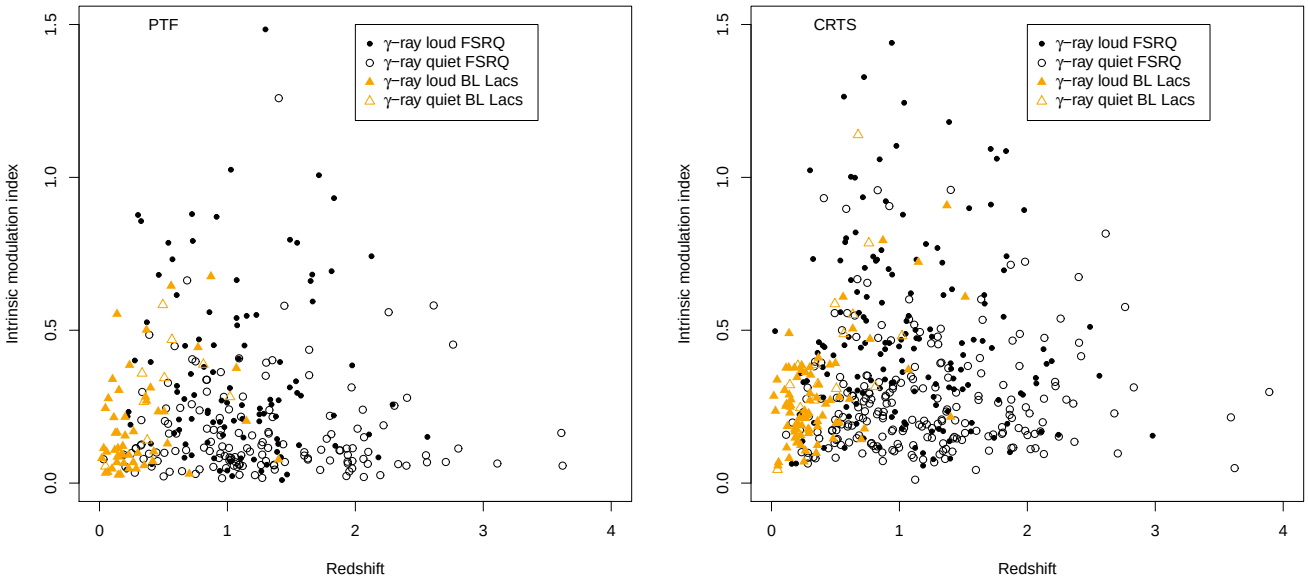

Figure 2. Intrinsic modulation index against the redshift for the PTF (left) and CRTS (right) samples. *Fermi*-detected FSRQs are shown with black filled circles, non-detected FSRQs with open black circles, *Fermi*-detected BL Lacs with filled orange triangles, and non-detected BL Lacs with open orange triangles.

Table 2. The mean intrinsic modulation indices and their 1σ errors in the PTF and CRTS samples for the various sub-populations used in the analysis.

Sample	γ-ray loud	γ-ray quiet	FSRQ	BL Lac	LSP	ISP	HSP
PTF	$0.201^{+0.015}_{-0.014}$	$0.096^{+0.015}_{-0.012}$	$0.215^{+0.023}_{-0.020}$	$0.149^{+0.015}_{-0.014}$	$0.277^{+0.035}_{-0.030}$	$0.199^{+0.038}_{-0.031}$	$0.096^{+0.017}_{-0.014}$
CRTS	$0.254^{+0.016}_{-0.015}$	$0.163^{+0.022}_{-0.019}$	$0.315^{+0.031}_{-0.027}$	$0.179^{+0.015}_{-0.014}$	$0.365^{+0.039}_{-0.035}$	$0.243^{+0.041}_{-0.034}$	$0.123^{+0.018}_{-0.015}$

the most likely value for the difference between the populations. These are listed in Table 3.

3.3 γ-ray detected vs. non-detected sources

Figure 4 shows the probability density of the mean intrinsic modulation index for the γ-ray detected and non-detected objects in the CRTS (top) and PTF (bottom) samples. The two distributions are not consistent with a single value and the γ-ray detected objects are more variable than the non-detected ones. Both PTF and CRTS give consistent results. We find that the most likely difference between the mean intrinsic modulation indices is more than 3σ from zero.

If we limit the likelihood analysis to objects with redshift $z < 2$ (the common range for the detected and non-detected samples), the difference between the means of the *Fermi*-detected ($m_{0,\mathrm{PTF}} = 0.230^{+0.023}_{-0.020}$ and $m_{0,\mathrm{CRTS}} = 0.302^{+0.026}_{-0.024}$) and non-detected ($m_{0,\mathrm{PTF}} = 0.072^{+0.013}_{-0.012}$ and $m_{0,\mathrm{CRTS}} = 0.161^{+0.027}_{-0.022}$) sources is still highly significant with the most likely difference of $-0.156^{+0.024}_{-0.048}$ for PTF and $-0.139^{+0.036}_{-0.035}$ for CRTS.

One caveat is that the sample we use is not statistically complete as it is a combination of the CGRaBS and *Fermi*-detected sources which have different selection criteria. Therefore we repeat the analysis using the CGRaBS sources only, which is an unbiased sample. In this case the difference between the γ-ray detected and non-detected objects is even larger (see Table 3). This is mainly due to *Fermi* being more sensitive to HSP objects which are less variable than the LSP sources that dominate the CGRaBS sample, as we show below.

3.4 FSRQs vs BL Lac objects

Figure 5 shows the probability density of the mean intrinsic modulation index for the FSRQs and BL Lac objects in the CRTS (top) and PTF (bottom) samples. Again, the two distributions are not consistent with a single value and the FSRQs are more variable than BL Lac objects. The most likely difference between the mean intrinsic modulation index is more than 3σ from zero for the CRTS sample and nearly 3σ from zero for the PTF sources. If we repeat the analysis for the CGRaBS sources only, the most likely difference between the two populations is less than 1σ (see Table 3).

If we constrain our likelihood analysis to objects with $z < 1$, we find that the means of FSRQs ($m_{0,\mathrm{PTF}} = 0.197^{+0.030}_{-0.025}$ and $m_{0,\mathrm{CRTS}} = 0.318^{+0.041}_{-0.035}$) differ from the BL Lacs ($m_{0,\mathrm{PTF}} = 0.152^{+0.026}_{-0.021}$ and $m_{0,\mathrm{CRTS}} = 0.189^{+0.027}_{-0.023}$) by less than 2σ in the PTF with the most likely differ-

Table 3. Most likely difference between the mean intrinsic modulation indices and their 1σ errors and significances for the various sub-populations tested.

Populations	PTF	Signif.	CRTS	Signif.
γ-ray loud vs. γ-ray quiet	$-0.103^{+0.020}_{-0.020}$	4.5σ	$-0.090^{+0.027}_{-0.025}$	3.0σ
CGRaBS γ-ray loud vs. quiet	$-0.116^{+0.030}_{-0.032}$	$> 5\sigma$	$-0.117^{+0.085}_{-0.073}$	4.1σ
FSRQ vs. BL Lac	$-0.065^{+0.025}_{-0.027}$	2.6σ	$-0.135^{+0.031}_{-0.034}$	4.6σ
CGRaBS FSRQ vs. BL Lac	$-0.011^{+0.041}_{-0.038}$	$< 1\sigma$	$-0.068^{+0.043}_{-0.042}$	1.6σ
LSP vs. ISP	$-0.076^{+0.049}_{-0.047}$	1.5σ	$-0.120^{+0.054}_{-0.053}$	2.1σ
LSP vs. HSP	$-0.178^{+0.034}_{-0.037}$	$> 5\sigma$	$-0.240^{+0.034}_{-0.037}$	$> 5\sigma$
ISP vs HSP	$-0.101^{+0.035}_{-0.041}$	3.1σ	$-0.119^{+0.038}_{-0.044}$	3.4σ

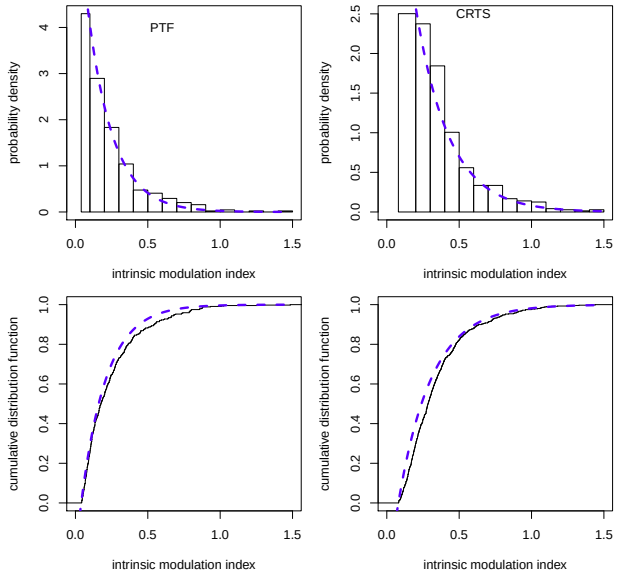

Figure 3. Top: Histogram of the maximum-likelihood intrinsic modulation indices $\overline{m}$ for the PTF sources with $\overline{m} > 0.04$ (left) and for the CRTS sources with $\overline{m} > 0.08$, normalized as a probability density. The blue dashed line shows an exponential function with a mean 0.18 (PTF) and 0.23 (CRTS), where the mean values are determined using the maximum-likelihood analysis. Bottom: Same data as in the top panel but shown with a cumulative distribution function.

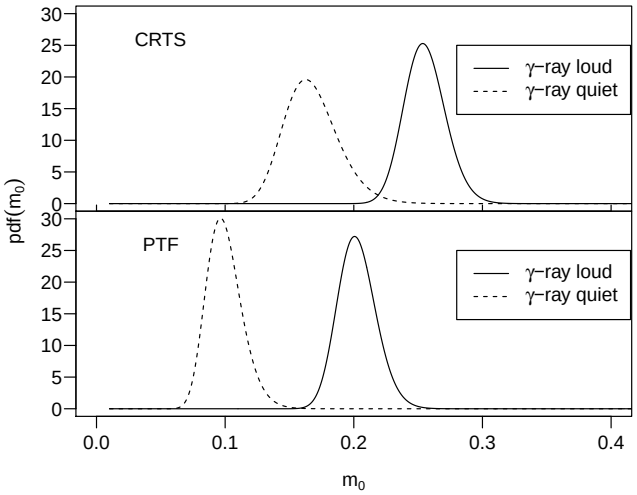

Figure 4. Probability density of the mean intrinsic modulation index for the γ-ray detected and non-detected objects in the CRTS (top) and PTF (bottom). Solid line is γ-ray loud objects. Dashed line is γ-ray quiet objects.

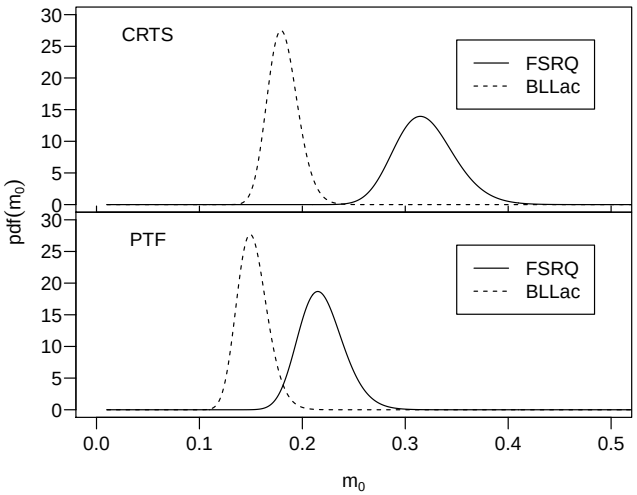

Figure 5. Probability density of the mean intrinsic modulation index for FSRQs and BL Lac objects in the CRTS (top) and PTF (bottom). Solid line is FSRQs, and dashed line is BL Lac objects.

ence of $-0.044^{+0.036}_{-0.037}$ and by about 2σ in the CRTS with the most likely difference of $-0.127^{+0.044}_{-0.047}$. The lower significance compared to the full sample is probably due to the smaller number of FSRQs used in the limited analysis. We test this by estimating the means of the FSRQs at $z < 1$ and at $z > 1$. The mean values at $z < 1$ are listed above and the most likely difference to the FSRQs at $z > 1$ ($m_{0,\mathrm{PTF}} = 0.235^{+0.037}_{-0.031}$ and $m_{0,\mathrm{CRTS}} = 0.309^{+0.050}_{-0.041}$) is less than 1σ for both the PTF sample with the most likely difference of $-0.038^{+0.043}_{-0.045}$ and the CRTS sample with the most likely difference of $-0.009^{+0.061}_{-0.059}$.

3.5 Division based on SED classification

Figure 6 shows the probability density of the mean intrinsic modulation index for the LSP, ISP and HSP sources in the CRTS (top) and PTF (bottom) samples. There is a clear trend in both data sets for the LSP sources to be more vari-

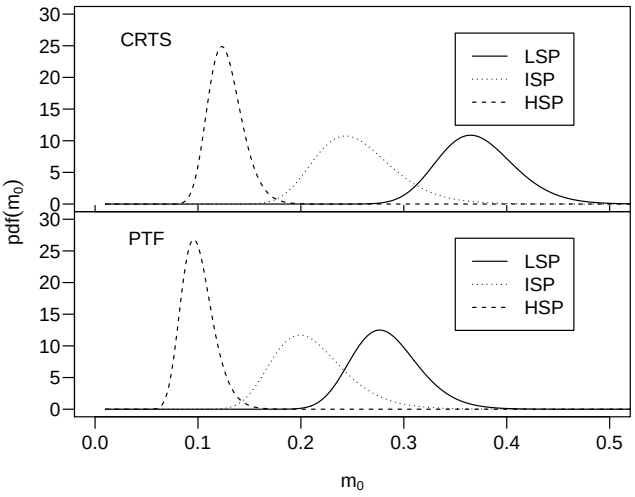

Figure 6. Probability density of the mean intrinsic modulation index for LSP, ISP and HSP objects in the CRTS (top) and PTF (bottom). Solid line is LSPs, dotted line is ISP objects, and dashed line is HSP objects.

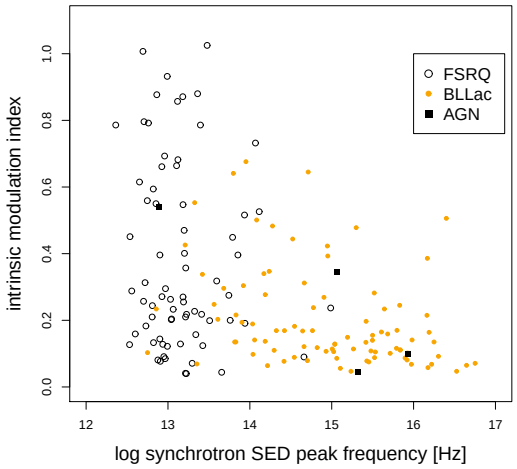

Figure 7. Intrinsic modulation index from PTF plotted against the peak frequency of the synchrotron component. FSRQs are shown with open circles, BL Lac objects with filled orange circles and AGN without optical classification with black squares.

able than the ISP and HSP sources. In the case of LSP vs. ISP sources we cannot distinguish the mean intrinsic modulation indices from each other within 2σ but the difference between LSP and HSP sources is highly significant. The mean intrinsic modulation index difference is more than 3σ from zero for both PTF and CRTS samples.

We also compare the intrinsic modulation index directly to the peak frequency of the synchrotron component. We use the peak frequencies used to determine the spectral classifications tabulated in the 2LAC catalog (Ackermann et al. 2011, B. Lott personal comm.). In Fig. 7 we plot the intrinsic modulation indices from the PTF sample against the peak frequencies. The HSP sources are less variable than the LSP sources that have a tail to much higher intrinsic modulation indices.

4 CORRELATION BETWEEN OPTICAL AND γ-RAY FLUXES

We use the method of Pavlidou et al. (2012) to study the correlation between PTF and γ-ray fluxes from the 2FGL catalog (Nolan et al. 2012). The strength of the correlation is quantified using the Pearson product-moment correlation coefficient r while the significance of the correlation is determined using simulated samples[6]. In order to account for the common redshift in the two variables, the sampling is done in the luminosity space. Because of this, we can only use objects with known redshifts in the correlation analysis. Additionally, we only use simultaneous PTF and 2FGL data and select those PTF sources that had at least 3 data points between 2008-Aug-4 and 2010-Aug-1 (the integration period for 2FGL) to calculate the intrinsic mean flux density. This results in a sample of 118 objects.

We first calculate the rest-frame optical luminosities for all our objects using

$$L(\nu) = S(\nu) 4\pi d^2 (1+z)^{1-\alpha}, \quad (2)$$

where $S(\nu)$ is the PTF intrinsic mean flux density in mJy, calculated using the likelihood method described in the previous section, d is the luminosity distance to the object, z is the redshift and α is the spectral index in the optical band defined as $S(\nu) \propto \nu^{\alpha}$. We do not have α values available for the individual sources and use values $\alpha = -1.5$ for LSP objects and $\alpha = -1.1$ for the HSP objects based on average values determined in Fiorucci et al. (2004). For sources without SED classification or ISP objects we use $\alpha = -1.3$. We note that the exact value of α does not have an effect on the significance of the correlation since we use the same value for both our data and the simulated samples.

The rest-frame γ-ray luminosities at $E_\gamma = 1\,\mathrm{GeV}$ are calculated using

$$L(E_\gamma) = (\Gamma - 1) F \left(\frac{E_\gamma}{E_0}\right)^{-\Gamma+1} 4\pi d^2 (1+z)^{\Gamma}, \quad (3)$$

where F is the photon flux above $E_0 = 1\,\mathrm{GeV}$ and Γ is the powerlaw index, both taken from the 2FGL. According to Nolan et al. (2012) (see their Fig. 6) the photon fluxes above $E_0 = 1\,\mathrm{GeV}$ are not affected by the spectral shape if the photon flux is larger than $0.4 \times 10^{-9}\,\mathrm{ph\,cm^{-2}s^{-1}}$. Our sample includes only four sources below this limit (3 LSP and 1 ISP) and therefore our sample is a nearly unbiased subset of a flux limited γ-ray sample.

We then construct simulated uncorrelated samples of the same size as our true sample by pairing optical and γ-ray luminosities of different sources. We move back to the flux-space by assigning a common redshift to the mixed pairs and estimate the strength of the correlation in the intrinsically uncorrelated sample using the Pearson correlation coefficient. Whenever the sample size allows, we use multiple

[6] The exact method for calculating the correlation coefficient is not critical because by estimating the significance through simulations, we ensure that the results do not depend on the distribution of the variables.

Table 4. Pearson product-moment correlation coefficient r for the γ-ray and optical flux correlations and the significance p of the correlations in the various subsamples. Number of sources N in each sample is also listed.

	r	p	N
All	0.39	0.0043	118
FSRQ	0.46	0.0031	76
BL Lac	0.69	5.8×10^{-5}	34
LSP	0.36	0.0229	69
ISP	0.94	0.0001	11
HSP	0.79	0.0005	19

redshift bins in the construction of the simulated samples. In this way we are able to obtain uncorrelated samples that are similar in dynamic range as our real observations. We repeat this procedure 10^7 times to estimate the significance (p-value) of the correlation. For a more detailed description of the method and recommendations for the redshift binning, see Pavlidou et al. (2012).

Figure 8 shows the 2FGL γ-ray photon flux against the PTF mean optical flux density for the various subclasses. The correlations, summarized in Table 4, are at least 3σ significant in all subclasses except for the LSP sources and all sources together. There are some caveats in the interpretation of the correlations. Firstly we do not include upper limits in the optical or γ-ray bands in the correlation estimation. As shown in Lister et al. (2011), this can have a significant impact on the result. We may be missing objects both in the upper left (faint in optical) and lower right (γ-ray faint) corners of the plot which will affect the strength and the scatter of the correlation, although not its significance. Secondly, we have not accounted for the host-galaxy emission in calculation of the optical fluxes, which may have an effect on the fluxes of the low redshift objects (e.g., Urry et al. 2000; Falomo et al. 2003). Furthermore, the optical emission in FSRQs can have a significant thermal component (e.g., Raiteri et al. 2007) which may increase the scatter in any correlations.

5 DISCUSSION

Using a large sample of sources from the PTF and CRTS optical surveys, we have studied the variability properties of γ-ray detected and non-detected objects, and of BL Lacs and FSRQs, in addition to dividing the sources based on their SED classification. We have determined the *intrinsic modulation index* for the different source populations and studied the flux - flux correlation between the optical and γ rays.

There are 637 sources in common in the PTF and CRTS samples. These include 320 sources with detected variability at more than 3σ level. A notable result seen in Figs. 4-6 is that the mean intrinsic modulation indices of the CRTS sources are systematically higher than in PTF. The number of data points in the two surveys are comparable but the CRTS data are more uniformly distributed over the five-year period considered here. This indicates that in order to detect the largest variability amplitudes long-term monitoring is needed. However, all our main findings are seen in both PTF and CRTS data sets, confirming the intrinsic nature of the differences between the sub populations.

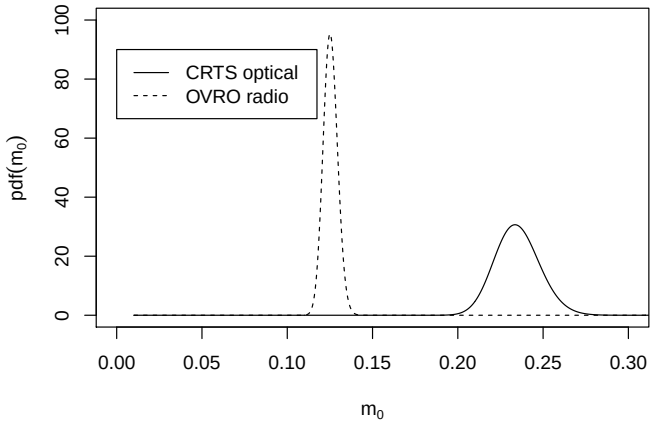

Figure 9. Probability density of the mean intrinsic modulation index for OVRO and CRTS data. Solid line is CRTS data (maximum-likelihood value and its 1σ error $m_0 = 0.234^{+0.014}_{-0.013}$). Dashed line is OVRO data ($m_0 = 0.125^{+0.004}_{-0.004}$).

Our sample was selected from the monitoring sample at OVRO so as to allow for comparison between the optical and 15 GHz radio variability. We use the CRTS sample for the comparison because it is larger (1244 objects) and the more uniform sampling is more similar to the OVRO observing cadence (on average 2 observations per week). The OVRO modulation indices are calculated based on four years of data (Richards et al. 2014). Fig. 9 shows the probability density of the mean modulation index for the overlapping CRTS and OVRO samples. The variability in the optical ($m_0 = 0.234^{+0.014}_{-0.013}$) is nearly twice as high as in the radio ($m_0 = 0.125^{+0.004}_{0.004}$). This is expected because the optical emission is thought to originate in smaller emission regions and be caused by higher energy electrons near the peak of the electron distribution.

5.1 Optical variability

One of our main results is that the *Fermi*-detected sources are more variable in optical than the non-detected objects. This has important implications for the identification of the unassociated objects in the *Fermi* catalogs. Up to 30% of the sources in the 2FGL catalog lack associations at other wavebands (Nolan et al. 2012). This is mainly because the source position errors are still fairly large and the 95% error circle can include multiple objects. In order to identify the correct counterpart for the γ-ray source some additional information is needed. Identifying unassociated sources has successfully been done by correlating the γ-ray properties with known source populations (Ackermann et al. 2012a) and by using data at various other wavelengths (e.g., Kovalev 2009; D'Abrusco et al. 2013; Massaro et al. 2013a,b; Maselli et al. 2013).

Ruan et al. (2012) showed how the variability of sources in optical catalogs can be used to identify the blazar coun-

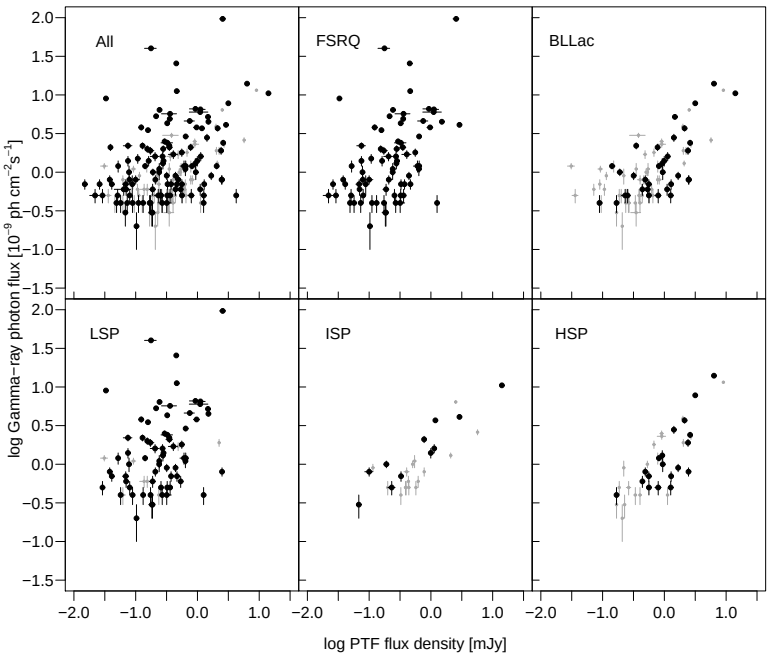

Figure 8. Integrated γ-ray photon flux with its 1σ uncertainty plotted against the intrinsic mean optical flux density and its 1σ uncertainty for all sources in our sample (top left), FSRQs (top middle), BL Lac objects (top right), LSPs (bottom left), ISPs (bottom middle), and HSPs (bottom right). Sources without redshifts are plotted in gray symbols and are not included in the calculation of the correlation.

terparts of the *Fermi* objects. They used optical data from the LINEAR asteroid survey and characterized the variability timescales and amplitudes of the objects. By selecting sources with variability characteristics similar to those of known blazars, they were able to recover 88% of the known associations in the 2FGL catalog, showing that identifying blazars using optical variability is an efficient tool. Our results agree with this conclusion and we suggest that the PTF and CRTS data can be used to aid in the identification of the unassociated sources (A. Mahabal et al. in prep.). One advantage of our modulation index method is that it can be used even for sources with only a few data points, as was explained in Sect. 3.

Our result agrees with the analysis of the OVRO 15 GHz radio data by Richards et al. (2011) that found the γ-ray detected objects to be more variable than the non-detected ones. They suggest that one possibility is that all the radio-loud objects are also γ-ray loud but were not detected by the LAT because they were not flaring during the first year of *Fermi* operations. This hypothesis was also suggested by Kovalev et al. (2009) who showed that the sources detected during the first three months of LAT monitoring were more variable in the 15 GHz Very Long Baseline Array data than the non-detected ones.

In addition, we divided our sources based on their optical classification into BL Lacs and FSRQs and based on their SEDs into LSP, ISP and HSP sources. When looking at the total sample we find the FSRQs to be significantly more variable than BL Lacs. This is mainly due to the location of the SED peak so that the lower variability in BL Lacs is driven by the less variable ISP and HSP sources. In fact, if we compare the CGRaBS sources only (dominated by LSP BL Lacs), or the *Fermi* -detected LSP BL Lacs and FSRQs, the difference between the two optical classes is significant only at the 1σ level. Similar results were obtained by Ikejiri et al. (2011) who studied the NIR variability in a sample of 42 objects. This could potentially be due to many of the LSP BL Lacs being intrinsically similar to FSRQs as suggested by Giommi et al. (2012, 2013), but falsely classified as BL Lacs due to the jet emission swamping any thermal emission.

A similar tendency for higher variability in the LSP sources was found in the γ-ray data in the 2nd LAT AGN catalog (Ackermann et al. 2011). They attribute this to the location of the high-energy peak with respect to the *Fermi* band. LSP sources observed by *Fermi* are observed at greater energies than the inverse Compton peak and therefore are produced by higher energy electrons which cool faster and vary more. HSP sources on the other hand are observed at lower energies than the peak and therefore would vary less. This is similar to what we see in the optical observations with respect to the synchrotron peak (e.g., Mastichiadis & Kirk 1997; Kirk & Mastichiadis 1999). Interestingly, Richards et al. (2011) found using 15 GHz data that BL Lac objects were more variable than FSRQs in the CGRaBS sample. This can at least partially be explained by the CGRaBS BL Lac sample being dominated by LSP objects which tend to vary more than the HSPs. When a gamma-ray–selected parent sample is used instead of CGRaBS, no significant difference in variability is found between FSRQs and BL Lacs, and a trend with greater variability in LSPs than HSPs is seen (Richards et al. 2014).

Bauer et al. (2009) used the Palomar QUEST survey to extract optical variability information for blazars and also found that FSRQs exhibit larger amplitude variations than the BL Lac objects. They suggest that this could be

due to higher jet power in the FSRQs which would allow them to produce larger flares. This agrees with the suggestion of Ghisellini et al. (1998) that more luminous objects have higher energy density and therefore cool faster which causes their synchrotron spectrum to peak at lower frequencies. Ghisellini et al. (1998) used this to explain the so called blazar sequence (Fossati et al. 1998) where the peak of the synchrotron and inverse Compton components shifts in frequency and luminosity depending on the source type. Subsequently, several issues have been identified with the original blazar sequence (e.g., Padovani 2007; Nieppola et al. 2008) and Ghisellini & Tavecchio (2008) updated their model to include the accretion disc differences between the objects. They suggest that the high power sources have an efficiently radiating accretion disc that contributes to their emission while the lower power BL Lac objects have an inefficient accretion disc. Recently Meyer et al. (2011) showed using larger samples that, instead of a simple sequence the FSRQs and BL Lacs have different loci in the jet power - synchrotron peak plane which can explain some of the differences in their observed properties. We may also be seeing an additional contribution from the accretion disc in the FSRQs in the optical band. Combining the effects of higher jet power, more efficient accretion disc, and higher electron energies at the optical band in FSRQs compared to BL Lacs can most likely explain the difference in variability we see in these objects.

5.2 Flux correlations

In addition to finding that the activity in the two bands is connected, we also find the simultaneous fluxes to be correlated. We find the correlation to have less scatter in BL Lacs than the FSRQs. This is opposite to what was seen by Arshakian et al. (2012) who used non-simultaneous data to study the optical - γ-ray flux correlation in 82 sources and found a significant correlation only in the FSRQs. We found that when testing for the correlation using the entire PTF data set without requiring simultaneous data, the scatter in the correlation was much larger. As suggested by Arshakian et al. (2012) use of non-simultaneous data can most likely explain the large scatter seen in their correlations.

If the γ-ray emission is produced by the synchrotron self-Compton (SSC) method, we would expect a tight correlation in the flux-flux space due to the same amount of Doppler-boosting in these regimes. In the case of external Compton emission, the high-energy component is more boosted which destroys a linear dependence (e.g., Dermer 1995). Additionally, there can be a large contribution from the external thermal photon field to the observed optical fluxes, hindering any correlations further. It is typically possible to model the SEDs of HSP sources using just a single SSC component while the FSRQs and LSP sources nearly always require an additional EC component (e.g., Lindfors et al. 2005; Abdo et al. 2010c, 2011; Böttcher et al. 2013).

Our observations are in good agreement with these models with the ISP and HSP sources showing a tighter correlation than the FSRQs. A Similar conclusion was drawn by Lister et al. (2011) based on a tight correlation between the γ-ray to radio flux ratio and the synchrotron peak frequency in a complete radio and γ-ray selected sample of 173 AGNs. One caveat in the comparison using radio data is that the radio and γ-ray emission are produced by very different energy electrons. The higher γ-ray to radio ratios in HSP objects in comparison to LSP sources seen in Lister et al. (2011) and in Nieppola et al. (2011) can be explained by the shifting of the synchrotron peak to higher frequencies in HSP objects, which decreases the amount of radio emission seen and increases the γ-ray dominance.

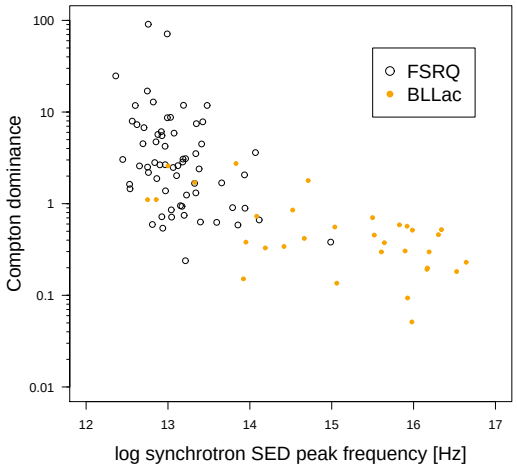

Figure 10. Compton dominance (ratio between γ-ray and PTF νF_ν) against the synchrotron peak frequency. Open circles are FSRQs and orange filled circles BL Lac objects.

Alternatively, the ratio between γ-ray and optical emission is nearly the same as the Compton dominance, defined as the ratio of the peak luminosity in the IC and synchrotron components. As in Pavlidou et al. (2012), we use the photon flux between 1 and 100 GeV tabulated in 2FGL to calculate the γ-ray flux density as

$$S_E(E_\gamma) = (\Gamma - 1)F\left(\frac{E_\gamma}{E_0}\right)^{(1-\Gamma)} \text{cm}^{-2}\text{s}^{-1}, \quad (4)$$

where Γ is the powerlaw index, F is the photon flux in units ph cm^{-2} s^{-1}, E_γ is the energy where we want to define the energy flux density (in our case 1 GeV) and E_0 is the lower limit in energy (1 GeV in our case). Strictly, this equation assumes the photon flux is integrated from E_0 to infinity, but due to the steep photon indices, the difference to limiting the equation at 100 GeV is less than 1%. Expressing this in the SED units in the rest frame of the source, we find

$$E_\gamma \cdot S(E_\gamma) = E_\gamma \cdot S_E(E_\gamma)(1+z)^\Gamma, \quad (5)$$

where E_γ is the energy at which to estimate the flux in erg (in our case 1.6×10^{-3} erg corresponding to 1 GeV). Similarly, we convert our simultaneous PTF mean intrinsic flux densities to rest frame SED units at the central frequency $\nu = 4.56 \times 10^{14}$ Hz (658 nm), which gives

$$\nu F_\nu = \nu S(\nu)(1+z)^{(1-\alpha)}, \quad (6)$$

where $S(\nu)$ is the flux density in erg cm^{-2} s^{-1} Hz^{-1}, and α is the spectral index in the optical band. We then calculate the ratio $(E_\gamma \cdot S(E_\gamma))/(\nu F(\nu))$ which we call the Compton dominance.

In Fig. 10 we plot the Compton dominance against the synchrotron peak frequency. The LSPs are much more Compton dominated than the HSPs as was also seen by Abdo et al. (2010c). They attribute this to the higher EC contribution in the LSP objects. This agrees very well with our flux-flux correlation result. Our results are also very similar to Finke (2013) who studied the Compton dominance in *Fermi* blazars by estimating the synchrotron and IC peak SED luminosities. Finke (2013) explain the trends seen in the plot with a simple model where the difference between the sources is due to magnetic field and energy density in the emission region, in addition to the viewing angle of the source.

Taking the connected variations in the two bands together with the flux-flux correlation is a strong indication for SSC origin of γ-ray emission in the HSP objects. However, we note that in individual sources and in individual flares the situation may be more complicated as shown in several detailed studies of individual sources (e.g., Marscher et al. 2010; Ackermann et al. 2012b; Nalewajko et al. 2012; Orienti et al. 2013).

6 CONCLUSIONS

We have studied the optical variability of AGN using large samples of objects from the PTF and CRTS surveys. We use a likelihood approach to calculate the intrinsic modulation index and a maximum likelihood method to study the differences between various source populations. Additionally, we studied the flux-flux correlation between the optical and γ-ray bands. Our main results can be summarized as follows:

(i) We find the *Fermi*-detected objects to be more variable than non-detected ones. This shows that the activity in the two bands is connected and that the optical variability can be used as a tool for identifying unassociated *Fermi* sources.

(ii) The FSRQs in our total sample are more variable than the BL Lac objects. This is likely due to the location of their synchrotron peak because the mean modulation indices of radio-selected CGRaBS FSRQs and BL Lacs or the *Fermi*-detected FSRQs and LSP BL Lacs do not differ significantly.

(iii) When dividing the objects based on their synchrotron peak location, we find the LSP objects to be more variable than the HSPs, with ISPs in between the two. This is similar to what is seen in the γ-ray band and can be due to differences in the electron energy in the observed bands.

(iv) We find a significant correlation between the optical and γ-ray fluxes which is tighter in the BL Lac objects. The FSRQs are also more Compton dominated than the BL Lacs. This is in accordance with models where the high-energy emission of the HSP and ISP sources can be modeled with a single SSC component while in FSRQs an additional EC component is required.

ACKNOWLEDGMENTS

We thank the referee, Tigran Arshakian, for useful comments that helped to improve the manuscript. T.H. thanks Elina Lindfors for useful discussions. T.H. was supported in part by the Jenny and Antti Wihuri foundation. V.P. is acknowledging support by the European Comission Seventh Framework Programme (FP7) through the Marie Curie Career Integration Grant PCIG10-GA-2011-304001 "JetPop" and the EU FP7 Grant PIRSES-GA-2012-31578 "EuroCal". The OVRO 40-m monitoring program is supported in part by NASA grants NNX08AW31G and NNX11A043G, and NSF grants AST-0808050 and AST-1109911. The National Radio Astronomy Observatory is a facility of the National Science Foundation operated under cooperative agreement by Associated Universities Inc. The CSS survey is funded by the National Aeronautics and Space Administration under Grant No. NNG05GF22G issued through the Science Mission Directorate Near-Earth Objects Observations Program. The CRTS survey is supported by the U.S. National Science Foundation under grants AST-0909182. This article is based on observations obtained with the Samuel Oschin Telescope as part of the Palomar Transient Factory project, a scientific collaboration between the California Institute of Technology, Columbia University, Las Cumbres Observatory, the Lawrence Berkeley National Laboratory, the National Energy Research Scientific Computing Center, the University of Oxford, and the Weizmann Institute of Science. It is also partially based on observations obtained as part of the Intermediate Palomar Transient Factory project, a scientific collaboration among the California Institute of Technology, Los Alamos National Laboratory, the University of Wisconsin, Millwakee, the Oskar Klein Center, the Weizmann Institute of Science, the TANGO Program of the University System of Taiwan, the Kavli Institute for the Physics and Mathematics of the Universe, and the Inter-University Centre for Astronomy and Astrophysics. This research has made use of the NASA/IPAC Extragalactic Database (NED) which is operated by the Jet Propulsion Laboratory, California Institute of Technology, under contract with the National Aeronautics and Space Administration.

REFERENCES

Abdo A. A. et al., 2010a, Nature, 463, 919
Abdo A. A. et al., 2010b, ApJ, 715, 429
Abdo A. A. et al., 2010c, ApJ, 716, 30
Abdo A. A. et al., 2011, ApJ, 736, 131
Ackermann M. et al., 2011, ApJ, 743, 171
Ackermann M. et al., 2012a, ApJ, 753, 83
Ackermann M. et al., 2012b, ApJ, 751, 159
Agudo I. et al., 2011, ApJ, 726, L13
Aller M. F., Aller H. D., Hughes P. A., 1992, ApJ, 399, 16
Arshakian T. G., León-Tavares J., Böttcher M., Torrealba J., Chavushyan V. H., Lister M. L., Ros E., Zensus J. A., 2012, A&A, 537, A32
Atwood W. B. et al., 2009, ApJ, 697, 1071
Bauer A., Baltay C., Coppi P., Ellman N., Jerke J., Rabinowitz D., Scalzo R., 2009, ApJ, 699, 1732
Bertin E., Arnouts S., 1996, A&AS, 117, 393
Bloom S. D., Marscher A. P., 1996, ApJ, 461, 657
Bloom S. D. et al., 1997, ApJ, 490, L145
Bonning E. et al., 2012, ApJ, 756, 13
Bonning E. W. et al., 2009, ApJ, 697, L81
Böttcher M., Reimer A., Sweeney K., Prakash A., 2013, ApJ, 768, 54
Chatterjee R. et al., 2012, ApJ, 749, 191

D'Abrusco R., Massaro F., Paggi A., Masetti N., Tosti G., Giroletti M., Smith H. A., 2013, ApJS, 206, 12
Dermer C. D., 1995, ApJ, 446, L63
Dermer C. D., Schlickeiser R., 1993, ApJ, 416, 458
Djorgovski S. G. et al., 2012, in T. Mihara, M. Serino, eds, The First Year of MAXI: Monitoring Variable X-ray Sources. p. 263
Drake A. J. et al., 2009, ApJ, 696, 870
Edelson R., Turner T. J., Pounds K., Vaughan S., Markowitz A., Marshall H., Dobbie P., Warwick R., 2002, ApJ, 568, 610
Falomo R., Carangelo N., Treves A., 2003, MNRAS, 343, 505
Fanaroff B. L., Riley J. M., 1974, MNRAS, 167, 31P
Finke J. D., 2013, ApJ, 763, 134
Fiorucci M., Ciprini S., Tosti G., 2004, A&A, 419, 25
Fitzpatrick E. L., 1999, PASP, 111, 63
Fossati G., Maraschi L., Celotti A., Comastri A., Ghisellini G., 1998, MNRAS, 299, 433
Ghisellini G., Tavecchio F., 2008, MNRAS, 387, 1669
Ghisellini G., Celotti A., Fossati G., Maraschi L., Comastri A., 1998, MNRAS, 301, 451
Giommi P., Padovani P., Polenta G., Turriziani S., D'Elia V., Piranomonte S., 2012, MNRAS, 420, 2899
Giommi P., Padovani P., Polenta G., 2013, MNRAS, 431, 1914
Hartman R. C. et al., 2001, ApJ, 558, 583
Healey S. E. et al., 2008, ApJS, 175, 97
Ikejiri Y. et al., 2011, PASJ, 63, 639
Jester S. et al., 2005, AJ, 130, 873
Kharb P., Lister M. L., Cooper N. J., 2010, ApJ, 710, 764
Kirk J. G., Mastichiadis A., 1999, Astroparticle Physics, 11, 45
Kovalev Y. Y., 2009, ApJ, 707, L56
Kovalev Y. Y. et al., 2009, ApJ, 696, L17
Kraus A. et al., 2003, A&A, 401, 161
Landoni M., Falomo R., Treves A., Sbarufatti B., Decarli R., Tavecchio F., Kotilainen J., 2012, A&A, 543, A116
Landt H., Bignall H. E., 2008, MNRAS, 391, 967
Law N. M. et al., 2009, PASP, 121, 1395
Lindfors E. J., Valtaoja E., M. T., 2005, A&A, 440, 845
Lister M. L. et al., 2011, ApJ, 742, 27
Mahabal A. A. et al., 2011, Bulletin of the Astronomical Society of India, 39, 387
Maraschi L., Ghisellini G., Celotti A., 1992, ApJ, 397, L5
Marscher A. P. et al., 2010, ApJ, 710, L126
Maselli A. et al., 2013, ApJS, 206, 17
Massaro F., D'Abrusco R., Giroletti M., Paggi A., Masetti N., Tosti G., Nori M., Funk S., 2013a, ApJS, 207, 4
Massaro F., D'Abrusco R., Paggi A., Masetti N., Giroletti M., Tosti G., Smith H. A., Funk S., 2013b, ApJS, 206, 13
Mastichiadis A., Kirk J. G., 1997, A&A, 320, 19
Meyer E. T., Fossati G., Georganopoulos M., Lister M. L., 2011, ApJ, 740, 98
Nalewajko K., Sikora M., Madejski G. M., Exter K., Szostek A., Szczerba R., Kidger M. R., Lorente R., 2012, ApJ, 760, 69
Nieppola E., Valtaoja E., Tornikoski M., Hovatta T., Kotiranta M., 2008, A&A, 488, 867
Nieppola E., Tornikoski M., Valtaoja E., León-Tavares J., Hovatta T., Lähteenmäki A., Tammi J., 2011, A&A, 535, A69
Nolan P. L. et al., 2012, ApJS, 199, 31
Ofek E. O., Frail D. A., Breslauer B., Kulkarni S. R., Chandra P., Gal-Yam A., Kasliwal M. M., Gehrels N., 2011, ApJ, 740, 65
Ofek E. O. et al., 2012a, PASP, 124, 62
Ofek E. O. et al., 2012b, PASP, 124, 854
Orienti M. et al., 2013, MNRAS, 428, 2418
Padovani P., 2007, Ap&SS, 309, 63
Pavlidou V. et al., 2012, ApJ, 751, 149
Raiteri C. M. et al., 2007, A&A, 473, 819
Rau A. et al., 2009, PASP, 121, 1334
Richards J. L., Hovatta T., Max-Moerbeck W., Pavlidou V., Pearson T. J., Readhead A. C. S., 2014, MNRAS in press
Richards J. L. et al., 2011, ApJS, 194, 29
Ruan J. J. et al., 2012, ApJ, 760, 51
Schlafly E. F., Finkbeiner D. P., 2011, ApJ, 737, 103
Shaw M. S. et al., 2013, ApJ, 764, 135
Sikora M., Begelman M. C., Rees M. J., 1994, ApJ, 421, 153
Urry C. M., Scarpa R., O'Dowd M., Falomo R., Pesce J. E., Treves A., 2000, ApJ, 532, 816
Wagner S. J., Witzel A., 1995, ARA&A, 33, 163
Wagner S. J. et al., 1995a, ApJ, 454, L97
Wagner S. J. et al., 1995b, A&A, 298, 688

Table 5. Sources in the PTF sample. The full table will be available in the online edition of the journal.

OVRO name	Right Ascension	Declination	*Fermi* association	Redshift	Redshift reference	Opt. Class	SED class	$\overline{m}$	S_0
CRJ0001−0746	00:01:18.03	−07:46:27.01	2FGLJ0000.9−0748	...	...	B	ISP	$0.089^{+0.023}_{-0.017}$	$0.446^{+0.011}_{-0.011}$
J0003+2129	00:03:19.35	21:29:44.40	...	0.45	1	A	...	< 0.146	$0.037^{+0.000}_{-0.000}$
J0005+0524	00:05:20.21	05:24:10.70	...	1.9	1	Q	...	< 0.014	$1.234^{+0.000}_{-0.000}$
J0006−0623	00:06:13.89	-06:23:35.30	...	0.347	1	B	...	$0.266^{+0.072}_{-0.050}$	$0.225^{+0.017}_{-0.017}$
J0006+2422	00:06:48.79	24:22:36.50	...	1.684	1	Q	...	< 0.112	$0.108^{+0.000}_{-0.000}$
J0010+2047	00:10:28.74	20:47:49.70	...	0.6	1	Q	...	$0.162^{+0.029}_{-0.024}$	$0.085^{+0.003}_{-0.003}$
J0010+1058	00:10:31.01	10:58:29.50	...	0.089	1	A	...	$0.094^{+0.027}_{-0.019}$	$4.015^{+0.117}_{-0.118}$
J0010+1724	00:10:33.99	17:24:18.80	...	1.601	1	Q	...	$0.090^{+0.014}_{-0.011}$	$0.646^{+0.011}_{-0.011}$
J0013−1513	00:13:20.71	−15:13:47.90	...	1.838	1	Q	...	< 0.119	$0.050^{+0.000}_{-0.000}$
J0013+1910	00:13:56.38	19:10:41.90	2FGLJ0013.8+1907	...	...	B	...	$0.392^{+0.045}_{-0.038}$	$0.185^{+0.009}_{-0.009}$

Columns are as follows: (1) OVRO Name; (2) RA; (3) DEC; (4) *Fermi* association; (5) redshift; (6) redshift reference where 1 is Healey et al. (2008), 2 is Abdo et al. (2010a), 3 is Ackermann et al. (2011), and 4 is Landoni et al. (2012); (7) optical classification where Q = FSRQ, B = BL Lac object, G = galaxy, A = Active galactic nucleus, N = Narrow line Seyfert I galaxy, and U = unidentified; (8) SED class from Ackermann et al. (2011); (9) Intrinsic modulation index and its 1σ error; (10) Intrinsic mean flux density and its 1σ error.

© 2013 RAS, MNRAS **000**, 1–13

Table 6. Sources in the CRTS sample. The full table will be available in the online edition of the journal.

OVRO name	Right Ascension	Declination	*Fermi* association	Redshift	Redshift reference	Opt. Class	SED class	$\overline{m}$	S_0
J0001−1551	00:01:5.33	−15:51:7.10	...	2.044	1	Q	...	< 0.130	$0.215^{+0.000}_{-0.000}$
CRJ0001−0746	00:01:18.03	−07:46:27.01	2FGLJ0000.9−0748	...	...	B	ISP	$0.327^{+0.057}_{-0.044}$	$0.458^{+0.028}_{-0.028}$
J0003+2129	00:03:19.35	21:29:44.40	...	0.45	1	A	...	< 0.252	$0.035^{+0.000}_{-0.000}$
J0004−1148	00:04:4.92	−11:48:58.40	...	...	...	B	...	$0.350^{+0.075}_{-0.059}$	$0.059^{+0.005}_{-0.004}$
J0004+2019	00:04:35.76	20:19:42.20	...	0.677	1	B	...	$1.139^{+0.793}_{-0.353}$	$0.298^{+0.165}_{-0.113}$
J0005−1648	00:05:17.93	−16:48:4.70	...	...	...	U	...	$0.082^{+0.022}_{-0.019}$	$0.419^{+0.009}_{-0.009}$
J0005+0524	00:05:20.21	05:24:10.70	...	1.9	1	Q	...	< 0.044	$1.383^{+0.000}_{-0.000}$
J0005+3820	00:05:57.18	38:20:15.20	2FGLJ0006.1+3821	0.229	1	Q	LSP	< 0.105	$0.267^{+0.000}_{-0.000}$
J0006−0623	00:06:13.89	−06:23:35.30	...	0.347	1	B	...	$0.387^{+0.072}_{-0.056}$	$0.308^{+0.023}_{-0.023}$
J0006+2422	00:06:48.79	24:22:36.50	...	1.684	1	Q	...	< 0.100	$0.130^{+0.000}_{-0.000}$

Columns are as follows: (1) OVRO Name; (2) RA; (3) DEC; (4) *Fermi* association; (5) redshift; (6) redshift reference where 1 is Healey et al. (2008), 2 is Abdo et al. (2010a), 3 is Ackermann et al. (2011), and 4 is Landoni et al. (2012); (7) optical classification where Q = FSRQ, B = BL Lac object, G = galaxy, A = Active galactic nucleus, N = Narrow line Seyfert I galaxy, and U = unidentified; (8) SED class from Ackermann et al. (2011); (9) Intrinsic modulation index and its 1σ error; (10) Intrinsic mean flux density and its 1σ error.